

# Ultrasound Speckle / Despeckle Image Decomposition for Tissue Analysis

José Seabra and J. Miguel Sanches

**Abstract** Speckle corrupting Ultrasound images depends on the acoustic characteristics of the observed tissues. De-speckling methods are usually employed to improve visualization and interpretation of anatomical details and the information encoded in speckle pattern is usually discarded. This information, however, may contain useful information for diagnostic purposes.

This chapter proposes a joint method to estimate the despeckled and speckle components from the ultrasound data for morphological and textural analysis of the tissues. The method is based on a two-step approach. In the first step a denoised image is computed and in the second step the speckle field is obtained from the despeckle data obtained on the first step and from the original image.

The despeckle image provides morphological and anatomical information of the region under analysis while the speckle field is suitable to compute textural information mainly related with tissue micro-structure.

The adequacy of the proposed decomposition method is assessed by using both synthetic and real data from distinct tissues. Several different case studies and applications are presented to illustrate the usefulness of the method for tissue characterization purposes.

---

José Seabra and J. Miguel Sanches  
Institute for Systems and Robotics and Department of Bioengineering from Instituto Superior Técnico / Technical University of Lisbon, Portugal e-mail: jseabra@ist.ist.utl.pt, jmrs@ist.utl.pt

## 1 Introduction

Ultrasound imaging has become a standard procedure for medical diagnosis worldwide, particularly in assessing arterial diseases [1,2]. Although diagnostic by using ultrasound imaging is considered a harmless technique and allows real-time non-invasive scanning of anatomical details, B-mode ultrasound (BUS) images are pervaded by a severe type of multiplicative noise, called *speckle*, that makes its interpretation a difficult process highly depending on the subjective appreciation of the operator.

The presence of speckle noise in such images has been documented since the early 1970s, when researchers such as Burckhardt [3], Wagner [4] and Goodman [5] described the fundamentals and statistical properties of speckle. Speckle is the primary factor which limits the contrast resolution in images, thereby hindering the detection of small, low contrast lesions and turning the interpretation of images into a challenging task. Speckle also limits the effective application of image processing and analysis algorithms for region, edge detection, segmentation and classification purposes.

There is described in the literature a large number of methods for speckle reduction either for medical ultrasound imaging [6] and other modalities involving coherent radiation such as synthetic aperture radar (SAR) [7] and LASER [8]. Such wide spectrum of techniques suggests that the problem remains a topic of interest for the image processing community and is far from being completely solved.

De-speckling is always a trade-off between noise suppression and loss of information, which is a critical issue specially when medical diagnosis is involved. Most of the work aims at removing noise for image quality improvement [9–13]. However, other works are also explore the information contained in the noise pattern for the extraction of echo-morphology and texture features for tissue analysis [14–17].

Ultrasound speckle [3] arises from constructive and destructive interferences between diffuse scatterers within a certain resolution cell. The most popular model to describe speckle formation is the fully speckle condition which considers a large number of scatterers whose reflected signals combine according a random walk process of component phasors sum. This speckle model implies a Rayleigh statistics for the envelope of the backscattered (amplitude) signal [18]. For what concerns the grey-level image appearance the Rayleigh distribution has shown to be a good approximation for modeling pixel intensities in homogeneous regions despite other distributions, including the K- [19], Nakagami [20], and Rician Inverse Gaussian [18], are more convenient, mainly when the image presents bright edges/transitions or strong isolated scatterers.

Speckle pattern is often referred as being multiplicative since its variance depends on the underlying signal intensity, meaning more noise power in brighter regions than in darker ones. Thus, de-noising methods based on the common *Additive White Gaussian Noise* (AWGN) observation model is not unappropriated to deal with this type of noise. Additionally, other methods have been proposed for de-noising and reconstruction based on median and adaptive filtering [21], wavelets [22], anisotropic diffusion [23] or other approaches [12,13].

This chapter presents a joint framework for image de-noising and speckle estimation which takes into account the multiplicative nature of the speckle signal. The de-noising procedure, that is usually an *ill-posed* [24] problem, may be tackled by using a Bayesian approach [25] which considers *a priori* information about the unknown noiseless image to be estimated.

The problem is formulated as an optimization task where a two-term energy function is minimized. In particular, the first term pushes the solution toward the observations (noisy pixel intensities) and the second regularizes it. Regularization is performed with a suitable edge-preserving prior, designated as *log-Euclidean*, which is used with a two-fold purpose: (i) being edge-preserving, and (ii) allowing to formulate the de-speckling task as a convex optimization problem. This method is also referred throughout this chapter as *Rayleigh-Log Total Variation* (RLTV) filter.

The main contribution of this chapter is to introduce a speckle reducing method based on a Bayesian approach [25] which assumes a Rayleigh observation model to describe the ultrasound pixel intensities and uses *a priori* information about the speckle-free image to be estimated. Such prior information, based on TV (*Total Variation*) [26], allows to regularize the solution by removing speckle while preserving the relevant anatomic details.

As previously mentioned, the information encoded in ultrasound speckle is often discarded but it is widely recognized that this phenomenon is dependent of the intrinsic acoustic properties of tissues [27]. The proposed method assumes the relevance of speckle for tissue analysis. Therefore, the method is designed to estimate both the noiseless and speckle components (images) from the ultrasound data. Hence, the de-speckling method, which will be further detailed provides clear images for medical interpretation and speckle fields for echo-morphology and texture characterization.

The remainder of this chapter is organized as follows. Section 2 describes the various steps of the speckle decomposition method, as depicted in Fig. 1. First, the mathematical formulation on the basis of the de-speckling algorithm is detailed, together with the optimization strategy adopted to find the noiseless solution. Subsequently, Section 2.1 describes the procedure to extract the speckle component from the estimated noiseless image. Furthermore, Section 2.2 presents a feature extraction procedure which enables to extract echogenicity and textural information from the image components previously obtained with the speckle decomposition method.

Section 3 exposes two types of results. The first exemplifies the speckle decomposition method, providing separation of BUS images into noiseless and speckle components. The adequacy of the proposed ultrasound image processing is assessed with both synthetic and real data. Second, insight on the usefulness of features extracted from noiseless and speckle images for tissue analysis is exploited through different case studies.

Finally, Section 4 concludes this chapter.

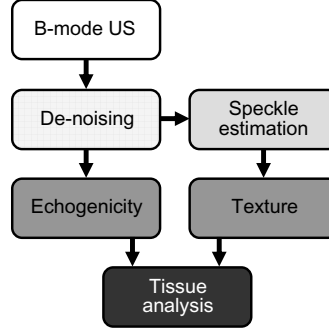


**Fig. 1** Ultrasound speckle decomposition framework.

## 2 Methods

The decomposition method comprises two main steps; i) speckle removal from the the noisy ultrasound image to obtained a cleaned noiseless image with morphological information about the organs and ii) speckle isolation, obtained form the noiseless and original noisy image, containing the textural information about the tissues. The first procedure, the more complex of both steps, is formulated in a Bayesian framework, where the unknown noiseless image  $\Sigma = \{\sigma_{i,j}\}$  is estimated form the noisy one,  $Y = \{y_{i,j}\}$ . The *Maximum a Posteriori* criterion (MAP) [28] is adopted to deal with the *ill-posedness* [24] nature of the problem. Therefore, the *despeckling* problem is formulated as an optimization task where an energy function is minimized,

$$\hat{\Sigma} = \arg \min_{\Sigma} E(\mathbf{Y}, \Sigma), \quad (1)$$

where

$$E(\mathbf{Y}, \Sigma) = E_d(\mathbf{Y}, \Sigma) + E_p(\Sigma). \quad (2)$$

$E_d(\mathbf{Y}, \Sigma)$ , called *data fidelity* term, pushes the solution toward the data and  $E_p(\Sigma)$ , called *prior* term, regularizes the solution by introducing prior knowledge about  $\Sigma$ .

The *data fidelity* term is the *log-likelihood* function  $E_d(\mathbf{Y}, \Sigma) = -\log(p(\mathbf{Y}|\Sigma))$  and by assuming statistical independence of the pixels,  $p(\mathbf{Y}|\Sigma) = \prod_{i,j=1}^{N,M} p(y_{i,j}|\sigma_{i,j})$  where  $p(y_{i,j}|\sigma_{i,j})$  is a Rayleigh distribution,

$$p(y_{i,j}|\sigma_{i,j}) = \frac{y_{i,j}}{\sigma_{i,j}^2} \exp\left(-\frac{y_{i,j}^2}{2\sigma_{i,j}^2}\right). \quad (3)$$

The estimation of  $\Sigma$  by simply using the *ML* criterion, corresponding to the minimization of  $E_d(\mathbf{Y}, \Sigma)$ , is an *ill-posed* problem in the Hadamard sense because the

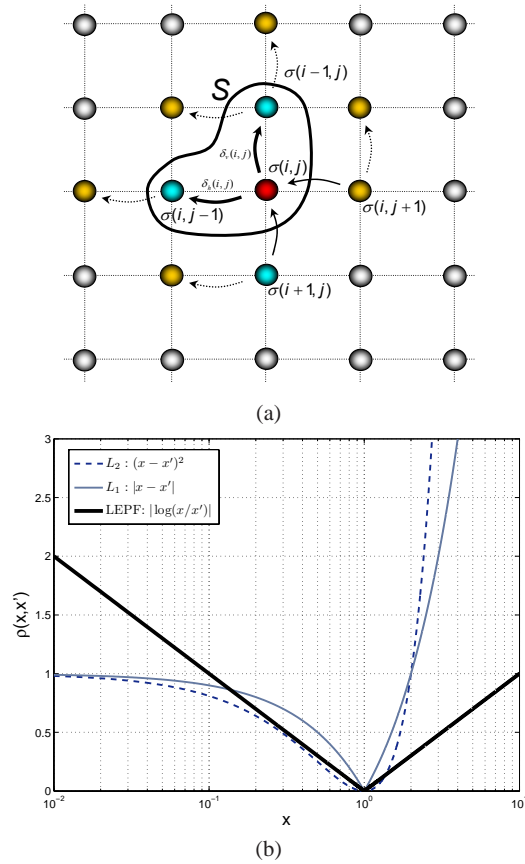


**Fig. 2** Log-Euclidean prior. a) 4-pixel neighboring system  $S$  and a 3-pixel *clique*. b) Comparison of different potential functions  $\rho(x, x')$  for a 2-pixel *clique* with  $x' = 1$ .

solution is not unique and it may not depend continuously on the data [24,29]. A regularization term is added to overcome this difficulty, turning the problem into a well-posed problem. The distribution  $p(\Sigma)$  introduces prior knowledge about the image to be estimated, thus regularizing and favoring smooth solutions. Even with a regularization term the minimization procedure of  $E(\mathbf{Y}, \Sigma)$  may be a difficult task, mainly when the energy function (2) is not convex. Therefore, two main issues must be taken into account in the designing of the prior function: i) the inclusion of realistic constraints and ii) convexity of the whole energy function.

The determination of a suitable prior distribution is difficult to attain, particularly in medical applications where straightforward assumptions about the prior distribution may lead to wrong diagnosis. The common assumption about these images is that they are band-limited, changing slowly in space except near the organs boundaries where abrupt transitions are expected. This prior information is difficult to

implement because the location of the transitions are unknown and must be estimated. Nevertheless,  $\Sigma$  can be modeled as a MRF (*Markov random field*) under the assumption that neighboring pixels are likely to have similar intensities, except if they are located at a transition.

From the Hammersley-Clifford theorem [30], the joint probability density function (PDF) of  $\Sigma$ , assuming that it is a MRF, is a Gibbs distribution

$$p(\Sigma) = \frac{1}{Z} \exp \left( -\alpha \underbrace{\sum_{i,j}^{N,M} \rho(c_{i,j})}_{\text{Gibbs energy}} \right), \quad (4)$$

where  $Z$  is the partition function [31],  $\rho(\cdot)$  is designated as *potential function* and  $c_{i,j}$  is the set of pixels involved in the  $(i,j)^{th}$  *clique* of the neighborhood system  $S$  defined in  $\Sigma$ , as it is shown in Fig. 2(a). The parameter  $\alpha$  models the interaction strength between neighbors. As  $\alpha$  increases, the prior becomes more significant than the data fidelity term, yielding a smoother solution.

Thus, the prior term is

$$E_p(\Sigma) = -\log(p(\Sigma)) = \alpha \sum_{i,j=1}^{N,M} \rho(c_{i,j}) + K, \quad (5)$$

where  $K$  is a constant. Differences between neighboring nodes are penalized by the prior term while the overall energy of the *cliques* is minimized, therefore contributing to speckle suppression.

Typical potential functions are based on the  $L_1$  (*Manhattan*) and  $L_2$  (*Euclidean*) norms [32], corresponding to  $\rho(c_{i,j}) = |\sigma_{i,j} - \sigma_{i-1,j}| + |\sigma_{i,j} - \sigma_{i,j-1}|$  and  $\rho(c_{i,j}) = (\sigma_{i,j} - \sigma_{i-1,j})^2 + (\sigma_{i,j} - \sigma_{i,j-1})^2$ , respectively. Particularly, when the  $L_2$  norm is used, the differences in neighboring pixel intensities are quadratically penalized. This potential function is able to efficiently remove the noise but is also attenuates or removes important anatomical details.

The Log-Euclidean prior, proposed in [33], is particular suitable in positive-constrained optimization problems, such as in this despeckling problem where the Rayleigh parameters to be estimated are  $\sigma_{i,j} > 0$ . This prior is based on the distance function  $\rho(x, x') = |\log(x/x')|$ , where  $x'$  is a neighboring pixel of  $x$ , which is in fact a metric because the following conditions hold: (i)  $\rho(x, x') \geq 0$ , (ii)  $\rho(x, x') = 0$  if and only if  $x = x'$ , (iii)  $\rho(x, x') = \rho(x', x)$  and  $\rho(x, x'') + \rho(x'', x') \geq \rho(x, x')$ . As mentioned before, the Log-Euclidean prior is here employed due to its edge-preserving properties and also because it turns the optimization problem formulated in (1) into a convex problem [34]. The potential function associated with this prior is

$$\rho(\mathbf{c}_{i,j}) = \sqrt{\log^2(\sigma_{i,j}/\sigma_{i-1,j}) + \log^2(\sigma_{i,j}/\sigma_{i,j-1})}, \quad (6)$$

where in each *clique* three nodes are involved,  $\mathbf{c}_{i,j} = \{\sigma_{i,j}, \sigma_{i-1,j}, \sigma_{i,j-1}\}$ . Fig. 2(b) displays the LEPF (*Log-Euclidean potential function*),  $|\log(x/x')|$  jointly with the common  $L_1 = |x - x'|$  and  $L_2 = (x - x')^2$  for a two pixel *clique* where  $x'$  is an unit intensity pixel,  $x' = 1$ . As it is observed the penalization introduced by the Log-Euclidean potential function (LEPF) when  $x$  and  $x'$  are similar is larger than the  $L_2$  prior and smaller than  $L_1$ , meaning better performance than the  $L_2$  prior to remove speckle but poorer than the  $L_1$  norm. However, when the difference between  $x$  and  $x'$  is large the penalization introduced by the LEPF is much smaller than the one introduced by the other two norms, thus leading to better preservation of the transitions which hypothetically contain relevant anatomical information. Additionally, for a given value of  $x'$ , when  $x$  goes to zero the penalization introduced by the  $L_1$  and  $L_2$  norms goes to a constant value while the penalization introduced by the LEPF continues to grow, which is very convenient in this case where the parameter of the Rayleigh distribution is strictly positive,  $\sigma_{i,j} > 0$ , but can be arbitrarily small.

The overall energy function, obtained from (2) is the following:

$$E(\mathbf{Y}, \Sigma) = \sum_{i,j} \left[ \frac{y_{i,j}^2}{2\sigma_{i,j}^2} + \log(\sigma_{i,j}^2) \right] + \alpha \sum_{i,j} \sqrt{\log^2 \left( \frac{\sigma_{i,j}^2}{\sigma_{i-1,j}^2} \right) + \log^2 \left( \frac{\sigma_{i,j}^2}{\sigma_{i,j-1}^2} \right)} \quad (7)$$

which is non-convex because, although the data fidelity term is convex, the prior term is concave. Its minimization is a difficult task mainly when gradient-descent methods are used [34]. However the following change of variable can be performed to transform (7) into a convex function,  $x = \log(\sigma^2)$ . The new convex energy function is,

$$E(\mathbf{Y}, \mathbf{X}) = \sum_{i,j} \left[ \frac{y_{i,j}^2}{2} \exp(-x_{i,j}) + x_{i,j} \right] + \alpha \underbrace{\sum_{i,j} \sqrt{(x_{i,j} - x_{i-1,j})^2 + (x_{i,j} - x_{i,j-1})^2}}_{TV(\mathbf{X})} + \varepsilon. \quad (8)$$

where the prior term, the TV of  $\mathbf{X} = \{x_{i,j}\}$ , is now convex because all of its terms are convex (second derivative is positive).

The stationary point of (8),  $\nabla_{\mathbf{X}} E(\mathbf{Y}, \mathbf{X}^*) = 0$ , that minimizes the energy function is iteratively computed by use of a line search [34] algorithm,

$$\tilde{\mathbf{X}}_{k+1} = \tilde{\mathbf{X}}_k + \omega_k \tilde{D}_k, \quad (9)$$

where the descent direction,  $\tilde{D}_k$ , is found with the Newton method [24]

$$\tilde{D}_k = H^{-1}(\tilde{\mathbf{Y}}, \tilde{\mathbf{X}}) \nabla_{\tilde{\mathbf{X}}} E(\tilde{\mathbf{Y}}_k, \tilde{\mathbf{X}}_k). \quad (10)$$

In (10),  $\tilde{\mathbf{X}}$  and  $\tilde{\mathbf{Y}}$  are column vectors obtained by lexicographic ordering of  $\mathbf{X}$  and  $\mathbf{Y}$  respectively. In addition,  $\nabla_{\tilde{\mathbf{X}}} E(\tilde{\mathbf{Y}}_k, \tilde{\mathbf{X}}_k)$  is the gradient column vector of  $E(\tilde{\mathbf{Y}}_k, \tilde{\mathbf{X}}_k)$  with respect to  $\tilde{\mathbf{X}}$  and  $H(\tilde{\mathbf{Y}}, \tilde{\mathbf{X}}) = [h_{i,j}]$  is the corresponding Hessian matrix where:

**Algorithm 1** convex optimization**Require:**  $\tilde{Y} \in \mathfrak{R}_0^+$ 

- 
- 1: *Initialize:*  $k = 0$ ,  $\tilde{Y}_0 = \log(\frac{\tilde{Y}^2}{2})$ ,  $\tilde{X}_0 = \log(\tilde{Y}_0)$ ,  $\eta = 10^{-6}$ ,  $s = 0.3$   
 $\varepsilon_N = 1$  (cooling),  $c_1 = 10^{-4}$  and  $\beta = 0.5$  (Armijo)
  - 2: **while**  $\varepsilon_N \geq \eta$  **do**
  - 3:   *compute*  $E(\tilde{Y}, \tilde{X}_k, \varepsilon_N)$  and  $\nabla E(\tilde{Y}, \tilde{X}_k, \varepsilon_N)$
  - 4:   **if**  $|\nabla_{\tilde{X}} E(\tilde{Y}, \tilde{X}_k, \varepsilon_N)| < \eta$  **then**
  - 5:      $\varepsilon_N \leftarrow s \times \varepsilon_N$
  - 6:     *compute*  $E(\tilde{Y}, \tilde{X}_k, \varepsilon_N)$  and  $\nabla_{\tilde{X}} E(\tilde{Y}, \tilde{X}_k, \varepsilon_N)$
  - 7:   **end if**
  - 8:   *compute*  $H(\tilde{Y}, \tilde{X})$  and  $\tilde{D}_k$
  - 9:    $\omega = 1$
  - 10:   **while**  $E(\tilde{Y}, \tilde{X}_k + \alpha \tilde{D}_k) > E(\tilde{Y}_k, \tilde{X}_k) + c_1 \omega \nabla_{\tilde{X}}^T E(\tilde{Y}, \tilde{X}_k) \tilde{D}_k$  **do**
  - 11:      $\omega \leftarrow \beta \omega$
  - 12:   **end while**
  - 13:    $\tilde{X}_{k+1} \leftarrow \tilde{X}_k + \omega \tilde{D}_k$
  - 14:    $k \leftarrow k + 1$
  - 15: **end while**
- 

$$h_{i,j} = \frac{\partial^2 E(\tilde{\mathbf{Y}}, \tilde{\mathbf{X}})}{\partial \tilde{x}_i \partial \tilde{x}_j}. \quad (11)$$

The Hessian matrix is a  $NM \times NM$  hepta-diagonal sparse matrix where for each pixel  $(i, j)$  six partial derivatives corresponding to its six neighbors,  $(\tilde{x}_{i,j}; \tilde{x}_{i,j})$ ,  $(\tilde{x}_{i,j}; \tilde{x}_{i,j-1})$ ,  $(\tilde{x}_{i,j}; \tilde{x}_{i,j+1})$ ,  $(\tilde{x}_{i,j}; \tilde{x}_{i-1,j})$ ,  $(\tilde{x}_{i,j}; \tilde{x}_{i+1,j})$ ,  $(\tilde{x}_{i,j}; \tilde{x}_{i-1,j+1})$ .

The iterative numerical technique adopted in (9) chooses, at each iteration  $k$ , a search direction by moving along  $\tilde{D}_k$  given by (10) while taking an appropriate step size  $\omega_k$ . One useful way to identify a step size that achieves adequate reductions in  $E(\mathbf{Y}, \mathbf{X})$  at minimal cost is by using the *Armijo* rule [35]. Given an initial step size,  $s > 0$  and  $\beta \in [0, 1]$  choose  $\omega_k$  to be the largest value in  $\{s, s\beta, s\beta^2, \dots\}$  such that:

$$E(\tilde{\mathbf{Y}}_k, \tilde{\mathbf{X}}_k + \omega_k \tilde{D}_k) \leq E(\tilde{\mathbf{Y}}_k, \tilde{\mathbf{X}}_k) + c_1 \omega_k \nabla_{\tilde{\mathbf{X}}}^T E(\tilde{\mathbf{Y}}_k, \tilde{\mathbf{X}}_k) \tilde{D}_k. \quad (12)$$

The Armijo rule is used with the following parameters:  $s = 1$ ,  $\beta = 0.5$  and  $c_1 = 10^{-4}$ . Hence, the strategy to choose  $\omega_k$  ensures a strictly decreasing sequence of energy values  $E()$  along the iteration process.

Moreover, a continuous variation strategy, also known as *cooling*, is used where a small decreasing constant  $\varepsilon$ , updated at each iteration, is added in order to deal with the non-smooth term of (8).

The main steps of the overall despeckling (RLTV) algorithm are listed in **Algorithm 1**. Finally, the estimated speckle-free image is obtained from  $\mathbf{X}$  by making  $\Sigma = \exp(\mathbf{X})$ .

## 2.1 Speckle Extraction

The previous section described the algorithm employed to estimate a noiseless image from B-mode ultrasound data. Here, the estimation of speckle is derived from the obtaining the denoised and original images.

Speckle corrupting the ultrasonic data is multiplicative in the sense that its variance depends on the underlying signal  $\Sigma = \{\sigma_{i,j}\}$ . Hence, the image formation model may be formulated as follows

$$y_{i,j} = \sigma_{i,j}\eta_{i,j}, \quad (13)$$

where  $\sigma_{i,j}$  is the intensity of pixel  $(i, j)$  of the despeckled image, while  $y_{i,j}$  and  $\eta_{i,j}$  are the observed (noisy) and speckle images, respectively.

In this model the speckle field  $N = \{\eta_{i,j}\}$  is independent of the signal as occurs in a common AWGN model where the noisy pixels,  $y = \sigma + \eta$ , are corrupted by noise,  $\eta$ , which is independent of the underlying signal  $\sigma$ . In the case of multiplicative model the operation is not additive but multiplicative as shown in (13). By assuming a Rayleigh distribution for the ERF image,

$$p(y|\sigma) = \frac{y}{\sigma^2} \exp\left(-\frac{y^2}{2\sigma^2}\right) \quad (14)$$

the distribution for  $\eta$  is

$$p(\eta) = \left| \frac{dy}{d\eta} \right| p(y) = \eta \exp\left(-\frac{\eta^2}{2}\right), \quad \eta \geq 0, \quad (15)$$

which shows that the noise image  $\eta$  is an unit parameter Rayleigh distribution independent of  $\sigma$ .

This result suggests that speckle does not carry significant echogenic information when studied locally, providing a more suitable source for describing textural characteristics.

The speckle field,  $N = \{\eta_{i,j}\}$ , is computed straightforwardly from the original ultrasound image,  $\mathbf{Y} = \{y_{i,j}\}$ , and the speckle-free version,  $\Sigma = \{\sigma_{i,j}\}$ , estimated from (13),

$$\eta_{i,j} = \frac{y_{i,j}}{\sigma_{i,j}}. \quad (16)$$

## 2.2 Features extraction

The decomposition method described in the previous sections will be used for tissue analysis where different types of features are computed from the estimated noiseless

and speckle components. Afterwards, we investigate the usefulness of such features for tissue analysis in different case studies.

The following features are considered:

### 2.2.1 Echogenicity index

The *echogenicity index*, referring to tissue distinct acoustic properties in a specific region, is represented by the averaged value  $\bar{\sigma}_W$  of local echogenicity values  $\sigma_{i,j}$  inside the  $n \times m$  window  $w = \{\sigma_{i,j}\}$  extracted from the de-speckled image  $\hat{\Sigma}$ .

### 2.2.2 Local Rayleigh estimators

In a previous work [36] the authors propose to compute features, to locally characterize the acoustic properties of tissues, directly from the estimated noiseless image,  $\Sigma = \{\sigma_{i,j}\}$ . This is done by using the analytical expressions for several statistics depending on the parameter of the distribution, estimated during the denoising operation. This means, we will estimate this statistics not directly from the observed noisy data but from the estimated parameters of the distribution that generates that data, in this case, Rayleigh distributions.

The statistics used in this work are the mean,  $\sigma_\mu(i, j)$ , median,  $\sigma_v(i, j)$ , *standard deviation* (SD),  $\sigma_\sigma(i, j)$ , and percentile 40,  $\sigma_{P_{40}}(i, j)$ . The percentile 40 refers to the percentage of pixels with echogenicity index lower than 40. This measure is particularly useful to identify low echogenic sites within a region of interest and is often used in the literature for characterize atherosclerotic plaques [37]. Their analytical expressions for the Rayleigh distribution are

$$\begin{cases} \sigma_\mu(i, j) = \sqrt{\frac{\hat{\sigma}(i, j)^2 \pi}{2}} \\ \sigma_v(i, j) = \sqrt{2 \log(2) \hat{\sigma}(i, j)^2} \\ \sigma_\sigma(i, j) = \sqrt{\frac{4-\pi}{2} \hat{\sigma}(i, j)^2} \\ \sigma_{P_{40}}(i, j) = 1 - \exp\left(\frac{-40^2}{2\hat{\sigma}(i, j)^2}\right). \end{cases} \quad (17)$$

### 2.2.3 Echogenicity decay

The intensity decay along depth is a common phenomenon occurring in diffuse liver disease [38] and is also visible in high-reflectivity tissues, like calcified carotid and coronary plaques [39]. The feature referring to *echogenicity decay*,  $s_d$ , is obtained by linear regression over the mean values of each line of the block  $k = \{\sigma_{m,n} : m = 1, \dots, M, n = 1, \dots, N\}$ ,  $\bar{\sigma}_m^k = \sum_{n=1}^N \sigma_{m,n}$ . It is obtained by minimizing the following cost function,

$$J = \sum_{m=1}^M (s_d m + b - \bar{\sigma}_m^k)^2. \quad (18)$$

Fig. 7(b.1)-Fig. 7(b.2) illustrate the distinct intensity profiles from de-speckled images of normal and pathologic livers, overlaid with the estimated *echogenicity decays* for each case.

### 2.2.4 Speckle-derived wavelet energies

The structure and directionality of speckle is hypothesized as being a relevant feature for tissue discrimination. Thus, suitable texture descriptors could be extracted from the isolated speckle field by considering the first Haar wavelet decomposition energies, particularly the approximation energy  $E_a$ , together with horizontal  $E_{dH}$  and vertical  $E_{dV}$  detail energies. Additionally, to quantify the relative detail in each direction, the ratio of horizontal to vertical detail energies,  $r_{HV} = E_{dH}/E_{dV}$  is computed, where  $r_{HV} \approx 1$  means that there is no predominant speckle directionality.

## 3 Experimental Results

The speckle decomposition method produces a despeckled image, carrying information about the local tissue echogenicity, and a speckle field, related to the structure and the characteristic pattern of tissues.

### 3.1 RLTV Filtering

In this section the performance of the despeckling method is evaluated by using a phantom image ( $w$ ) depicted in Fig. 3(a). The pixel values of this image are used to generate the log-compressed noisy image  $z$ , displayed in Fig. 3(b), that simulate the B-mode ultrasound image acquired by the scanner. The denoised image,  $\sigma$ , obtained with the RLTV algorithm is displayed in Fig. 3(c).

Pixel intensity diagonal profiles of images  $w$ ,  $z$  and  $\sigma$  are presented in Fig. 3(d). Moreover, in Fig. 3(e) the Rayleigh distributions obtained with averaged parameters computed in  $\sigma(W_1)$ ,  $\sigma(W_2)$ ,  $\sigma(W_3)$  are overlapped with data histograms in  $z(W_1)$ ,  $z(W_2)$  and  $z(W_3)$ . As it is observed in Fig. 3(d) and Fig. 3(e), the algorithm is able to correctly estimate the Rayleigh local parameters used to produce the phantom image.

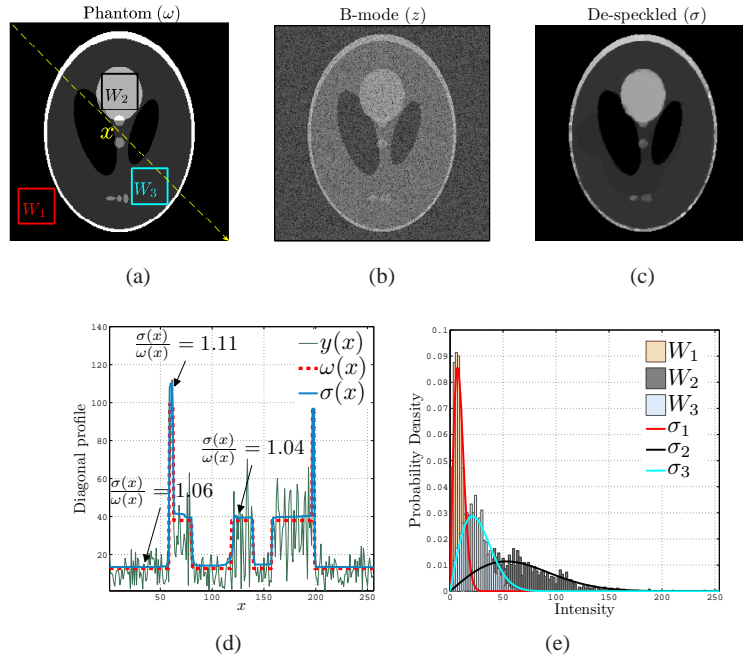
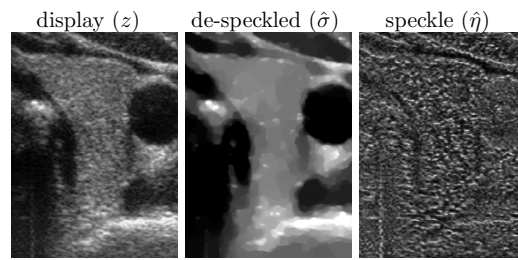


**Fig. 3** (a-c) RLTV filtering in a phantom image. (d) Diagonal profiles of (a-c). (e) PDFs and data histograms.

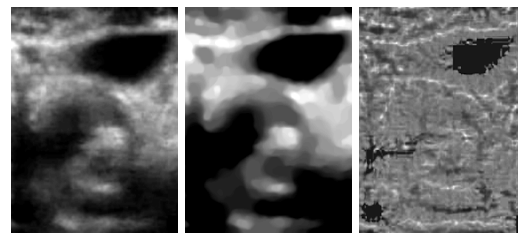
### 3.2 Filters Comparison

Moreover, we compare the speckle reduction results of the proposed de-noising method (RLTV) with other related work. From the view point of filter comparison it is important to study distinct filtering approaches rather than making a biased description of speckle suppression techniques. Hence, we have collected a set of techniques based on distinct concepts and formulations. In particular, we have used linear filters, such as the LSF (*Linear Scaling Filter*) [40], the pixel-wise adaptive Wiener method (WIE) [41] and the LHMAF (*Linear Homogeneous Mask Area Filter*) [42], non-linear filters, namely the MF (*Median filters*) [43] and the MHOPNF (*Maximum Homogeneity Over Pixel Neighborhood Filter*) [44], diffusion filters, including the ADF (*Anisotropic Diffusion Filter*) and the SRADF (*Speckle Reducing Anisotropic Diffusion Filter*) [23], wavelet filtering such as the WAVF (*WAVElet-based Filter*) and other more recent and sophisticated strategies, including the NLMF (*Non-Local Means Filter*) [13], the SBF (*Squeeze Box Filter*) [12], the MGF (*Modified Gabor Filter*) [45], the WRMLF (*Weighted Rayleigh Maximum Likelihood Filter*) [46].

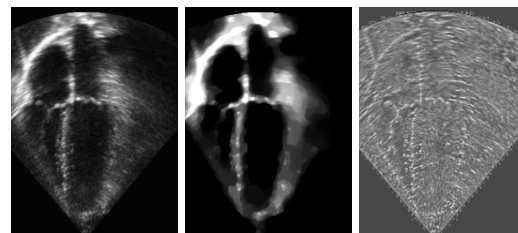
For medical ultrasound images, quality can be objectively assessed in terms of performance in clinically relevant tasks such as lesion detection, segmentation and



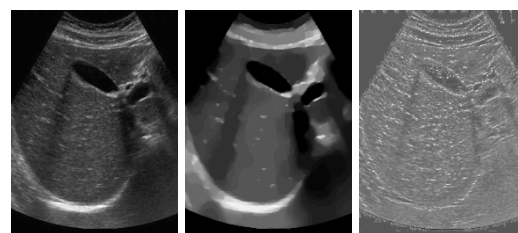
(a)



(b)

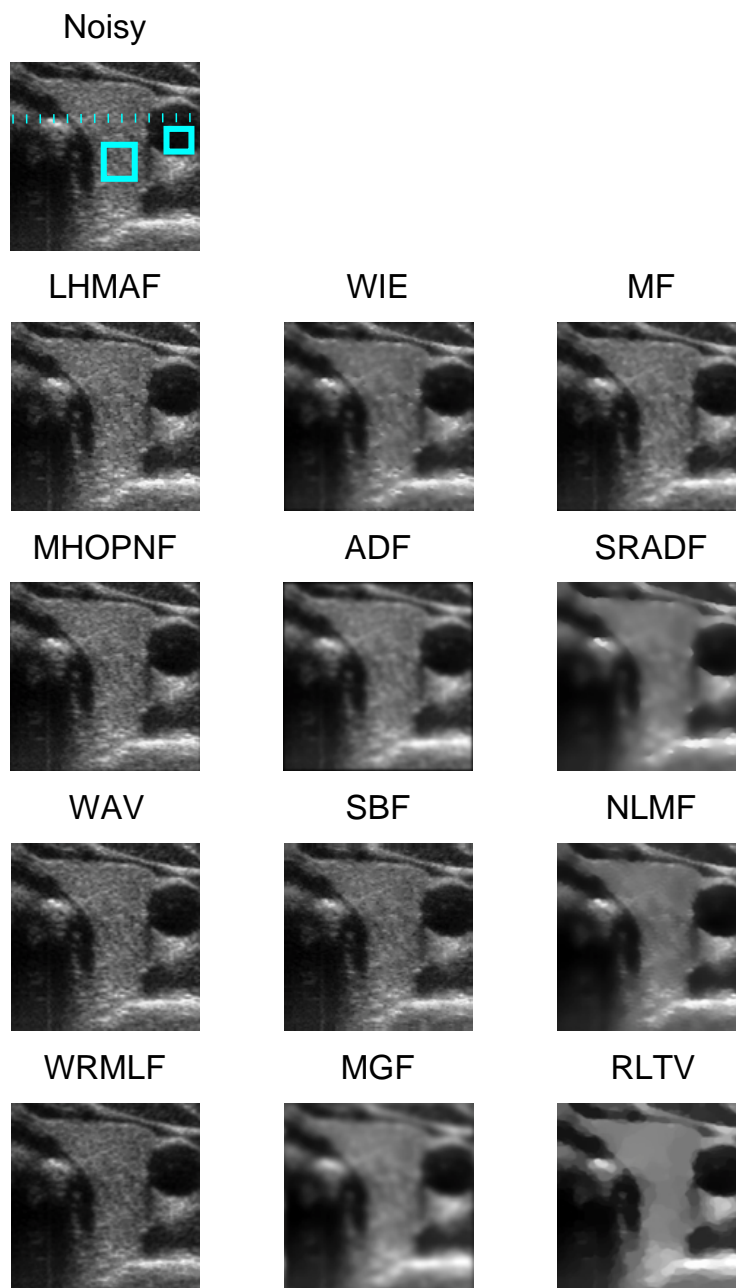


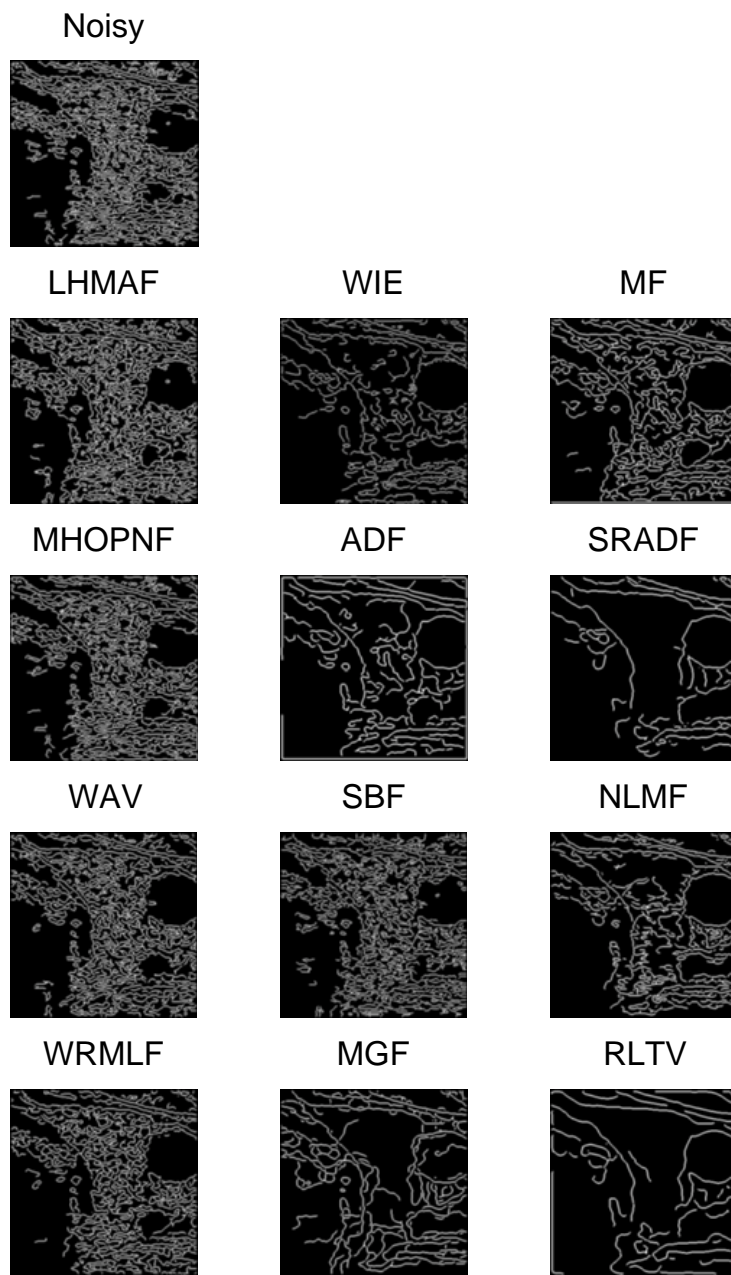
(c)



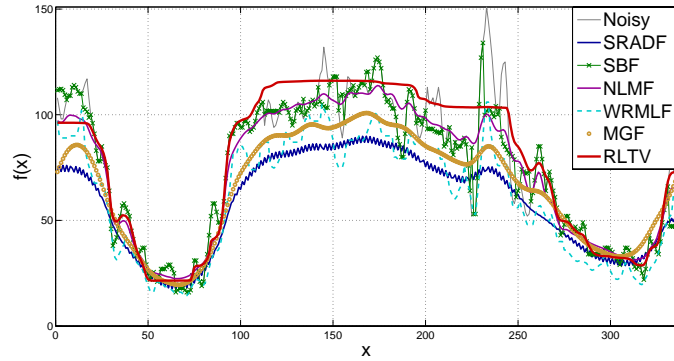
(d)

**Fig. 4** Ultrasound speckle decomposition method applied to different tissue types.

*(a)*



(b)



(c)

**Fig. 5** Comparison of the proposed RLTV filter and other approaches described in the literature, according to de-speckled images (a), edge maps (b) and image intensity profiles (c).

**Table 1** Comparison of filters performance using different FOM.

Filter	Figures of Merit (FOM)									
	$\mu_1^{100.52}$	$\mu_2^{18.23}$	$\sigma_1^{19.56}$	$\sigma_2^{9.18}$	$SSNR_1^{5.14}$	$SSNR_2^{1.99}$	PBenf	PUnif	t (s)	
LSF	100.32	18.24	10.21	6.91	9.82	2.64	1.11E-016	0.063	0.31	
LHMAF	102.64	19.72	19.19	8.91	5.35	2.21	2.22E-016	0.26	333.29	
WIE	100.26	18.00	11.40	6.91	8.80	2.60	2.22E-016	0.13	0.082	
MF	99.98	17.67	12.32	7.03	8.11	2.51	4.44E-016	0.083	6.22	
MHOPNF	100.49	18.24	16.49	8.30	6.10	2.20	2.22E-016	0.074	6.57	
ADF	100.32	18.25	10.27	6.92	9.77	2.64	2.22E-016	0.06	8.00	
SRADF	78.93	14.82	5.87	5.24	13.44	2.83	3.33E-016	0.42	4.31	
WAV	100.53	18.23	16.75	8.28	6.00	2.20	3.33E-016	0.079	1.04	
SBF	99.79	18.32	16.11	8.81	6.19	2.08	0	0.12	2.33	
NLMF	99.71	18.36	8.44	6.33	11.82	2.90	0.11	0.12	380.90	
WRMLF	81.52	14.37	12.71	6.054	6.41	2.37	5.55E-016	0.017	10.98	
MGF	88.33	16.26	7.03	5.74	12.56	2.83	3.33E-016	0.16	1.16	
RLTV	102.09	17.55	5.05	6.66	21.61	2.63	9.22E-014	0.089	192.07	

classification [47]. In the synthetic case, where the original images are available, a number of quantitative measures aiming at comparing the outcome of different filters can be studied, however dealing with real images poses some limitations. As a consequence, we assess the quality of each filter result according to three different criteria, including visual inspection, edge maps obtained from the de-noised images and quantitative criteria. Image quality in terms of visual inspection refers to contrast enhancement, speckle pattern suppression and edge-preservation. Moreover, the computation of edge maps foresees the application of segmentation algorithms in the noiseless images. Given this, an edge map which contains most of the anatomical details and very few outliers will theoretically produce the best segmentation results. Finally, we have used some quantitative measures, namely the SSNR (*Speckle*

*Signal to Noise Ratio*) [4], and the MPVR (*Mean Preservation Variance Reduction*). The latter can be assessed by computing the mean and variance in different regions within the image. The closer the computed mean within the noiseless and original image is, and the lower the variance, the better the filtering method is. Moreover, we use a test of reasonableness (naturalness) of each filter outcome. The application of some filters could lead to artificial images, although visually appealing in terms of speckle suppression and edge enhancement. Knowing that the first digit of the gradient magnitude in natural images follows the Benford law [48,49] we perform the Kolmogorov-Smirnov conformity test using the Benford law as well as the uniform distribution. If the Benford law-based test is close to 0 this means that the filter outcome produces a natural image.

Moreover, the computational efficiency of speckle removal filters, as these methods are supposed to be part of real time medical applications, becomes an unavoidable need. All the filters were implemented in Matlab and computed on an Intel Core 2 CPU @ 1.66GHz.

The effectiveness of the proposed RLTV filter is compared with other state-of-the-art methods, using a real ultrasound image of the thyroid. First, we show the outcomes of each filter in Fig. 5(a). From visual inspecting the noiseless images it becomes clear that the best results are obtained with the SRADF, NLMF and RLTV filter, according to efficient speckle suppression in homogeneous regions and excellent edge-preservation of relevant anatomical details. Some other methods, such as the MGF and the ADF are capable of removing most of speckle but they tend to blur the image.

Moreover, because de-speckling is often used as a pre-processing step for segmentation purposes, we have computed edge maps from each filter outcome using the Canny detector [50]. These results are depicted in Fig. 5(b). As it can be observed, the edge maps obtained from the SRADF and RLTV filter provide contain the most relevant edges in the image, particularly the ones that allow to outline the thyroid, while removing outlier edges.

Finally, Fig. 5(c) presents the image intensity profiles of some filters along a path marked in Fig. 5(a). This result reinforces the regularization effect produced by the RLTV filter, which is clearly able to eliminate most of the noise causing intensity variability while keeping abrupt intensity transitions due to transitions.

Filter comparison is also evaluated from a quantitative viewpoint. Table 1 presents some quantitative measures obtained for each filter outcome, using different FOM. Some of these FOM are computed from the marked regions in Fig. 5(a). A detailed observation enables to conclude that the RLTV method provides excellent results in terms of mean preservation and standard deviation reduction, while it outperforms other methods in terms of SSNR.

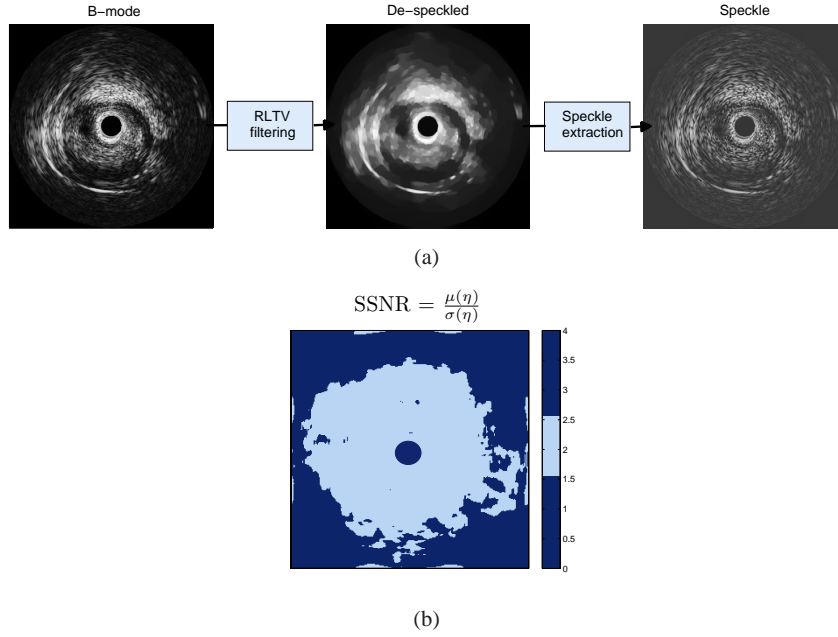


**Fig. 6** (a) Despeckled and speckle component estimates obtained from BUS IVUS image. (b) SSNR map computed over the speckle field  $\hat{\eta}$ .

### 3.3 Speckle Decomposition

In the previous experiment we have demonstrated the excellent speckle suppression and edge-preserving properties of the proposed RLTV filter. Here, we investigate the incorporation of such method into the so-called speckle decomposition method, providing not only the filter outcome but also a speckle field.

Fig. 4 presents different examples of the application of the proposed ultrasound speckle decomposition algorithm in different image types. To investigate the robustness of the despeckling method we have used ultrasound data from different structures and tissues (see Fig. 4), including thyroid (a), carotid artery (b), heart (c) and liver (d). Optimization results were obtained in 67(109.9s), 50(82.2s), 55(92.5s) and 61(101.6s) iterations, respectively. These results illustrate the ability of the RLTV algorithm to deal with different types of real images.

To complete this set of experiments related with speckle image decomposition, an example with *intra-vascular ultrasound* (IVUS) image of the coronary artery is provided in Fig.6(a). Additionally, the *Speckle Signal-to-Noise Ratio* (SSNR) is computed within a sliding window across the whole speckle image and the SSNR map is shown in Fig. 6(b). A precursor study [3] conducted in real ultrasound images, showed experimentally that when fully developed speckle occurs, the SSNR is in the range of 1.5 to 2.5. Given this, it is observed that the speckle field has sta-

tistical properties resembling a Rayleigh distributed signal, which strongly suggests the likelihood of the assumption of the Rayleigh observation model for the RLTV despeckling method.

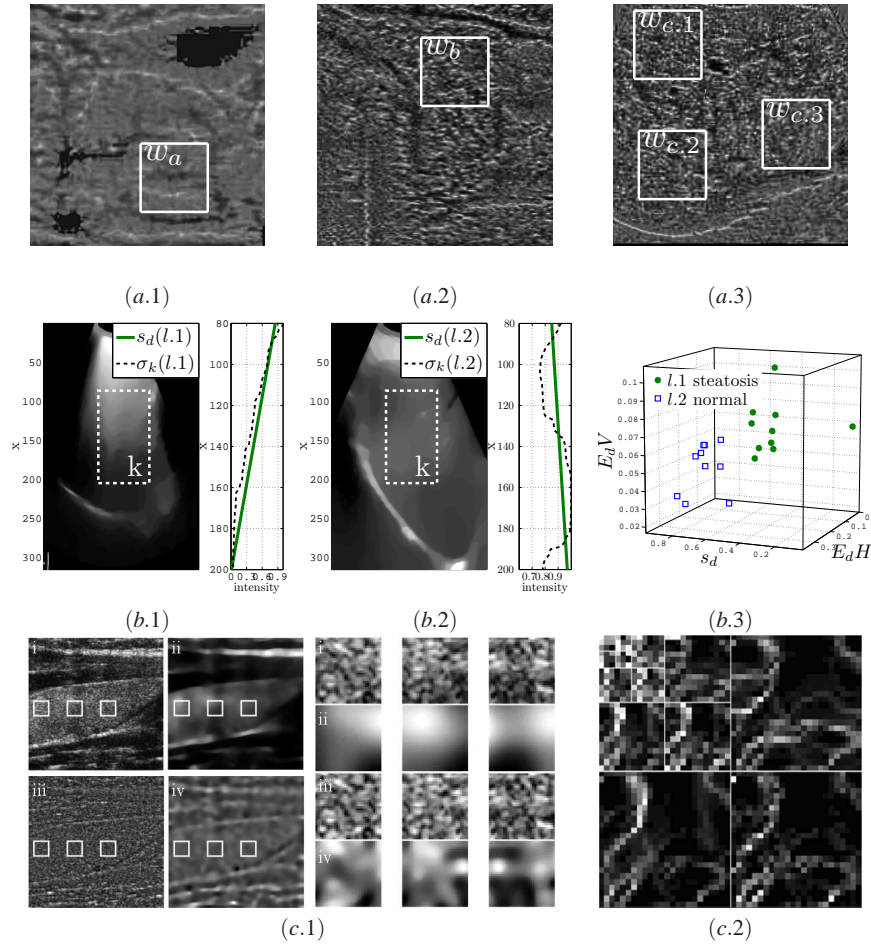


**Fig. 7** Feature extraction based on ultrasound speckle decomposition applied to different case studies. (a) first Haar wavelet energies based on speckle from plaque (1), thyroid (2) and liver (3). (b) feature based on *echogenicity decay* (1-2) and feature space of normal and steatotic livers. (c) Sample extraction from noiseless and speckle components, obtained from thyroid images (1); wavelet decomposition from speckle field (2).

Results of the speckle decomposition method have just been presented. Hence, it is now important to show that the outcomes of the proposed method are useful image sources of information for tissue analysis. Consequently, we present different

case studies using distinct ultrasound data:

**Evidence of tissue-dependent textural features:** the speckle field of ultrasound images from different tissue types, in particular of carotid plaque, thyroid and liver (Fig. 7(a)) are used to show that the energies associated with the first wavelet decomposition fields with Haar functions,  $E_a$ ,  $E_d$  and  $r_{HV}$ , differ significantly from one anatomical structure to another, as well as from one tissue area to another. In particular, the wavelet energies and energy ratios are (see Fig. 7(a)):  $E_a(w_a)=99.6$ ,  $E_d(w_a)=0.4$ ,  $r_{HV}(w_a)=2.8$ ;  $E_a(w_b)=95.4$ ,  $E_d(w_b)=4.6$ ,  $r_{HV}(w_b)=4.7$ ;  $E_a(w_{c.1})=92.3$ ,  $E_d(w_{c.1})=7.7$ ,  $r_{HV}(w_{c.1})=2.3$ ;  $E_a(w_{c.2})=94.3$ ,  $E_d(w_{c.2})=5.7$ ,  $r_{HV}(w_{c.2})=3.1$ ;  $E_a(w_{c.3})=96.3$ ,  $E_d(w_{c.3})=3.7$ ,  $r_{HV}(w_{c.3})=2.1$ .

**Liver steatosis binary classification:** a Bayes classifier trained with features related to *echogenicity decay* (see Fig. 7(b)) and wavelet energies is used in a binary classification problem. Features were extracted from a dataset of 20 livers, which were clinically validated as normal or steatotic (with abnormal lipid retention) [51], yielding the following feature set and values: for normal liver,  $\bar{s}_d=0.48$  (0.18)  $\bar{E}_dH=9.79$  (2.68)  $\bar{E}_dV=6.78$  (1.63); and for fatty liver,  $\bar{s}_d=0.80$  (0.11)  $\bar{E}_dH=19.97$  (4.54)  $\bar{E}_dV=4.66$  (1.61). Results, given in terms of sensitivity ( $S=1.00$ ) and specificity ( $K=0.95$ ), support the usefulness of features extracted both from the noiseless and speckle image sources for a specific tissue classification problem.

**Subject identification based on thyroid ultrasound data:** a subject identification problem based on thyroid tissue ultrasonic data was performed [52], considering a population of 10 subjects (several samples per subject). Again, features were extracted from both the estimated de-speckled image (echogenicity index) and speckle field (wavelet energies) as depicted in Fig. 7(c). Subsequently, the estimated feature set was used for training a bayesian classifier. Sensitivity results obtained for the problem of subject identification were:  $S=0.79$ , with echogenicity index features,  $S=0.70$ , with wavelet energies and  $S=0.94$  with a combination of both. Again, this example shows that distinct feature values can be obtained from thyroid tissue on the basis of the proposed ultrasound speckle decomposition method.

## 4 Conclusions

This chapter describes a new strategy for decomposing ultrasound B-mode images into its noiseless and speckle components, as well as, a new state of the art algorithm for despeckling.

First, a suitable de-noising algorithm is presented which aims at providing clearer yet edge-preserving images for medical interpretation. Subsequently, because speckle has multiplicative nature, an image containing the speckle pattern is estimated after knowing the corresponding noiseless image.

The adequacy of the RLTV filtering method has been compared with other filters, and afterwards established through synthetic examples and ultrasound images having different types. Moreover, as theoretically expected, an example using IVUS data, clearly shows that the speckle field has statistical properties resembling a Rayleigh distributed signal.

Furthermore, we have computed different features from noiseless and speckle image sources, arguing that such information is useful for tissue analysis. Hence, we have shown the convenience of working with the estimated echogenicity and textural features for tissue description through distinct real cases.

The first study is conducted to illustrate how features computed from the speckle field differ from a tissue to another and even within the same tissue. Wavelet detail and approximation energies together with the relative directional energy ratio have shown to be relevant tissue descriptors. The second and third examples use features extracted both from noiseless and speckle image sources. In particular, the second study uses a feature computed from the despeckled image (echogenicity decay) which is very convenient in the investigated two-class problem. In the two classification problems presented, the use of information resulting from the proposed speckle decomposition procedure leads to high classification scores.

Thus, we have shown that the proposed algorithm is able to provide more suitable images for visual diagnosis as well as useful sources of information for tissue analysis in different clinical scenarios.

## References

1. T. Nelson, D.H. Pretorius, D. Downey, and A. Fenster. *Three-Dimensional Ultrasound*. Lipincott Williams & Wilkins, Apr 1999.
2. D. Lamont et al. Risk of cardiovascular disease measured by carotid intima-media thickness at age 49-51: lifecourse study. *British Medical Journal*, 320(7230):273–278, 2000.
3. C. Burckhardt. Speckle in ultrasound B-mode scans. *IEEE Transactions on Sonics and Ultrasonics*, SU-25(1):1–6, Jan 1978.
4. R. F. Wagner, S. W. Smith, J. M. Sandrik, and H. Lopez. Statistics of Speckle in Ultrasound B-Scans. *IEEE Transactions on Sonics and Ultrasonics*, 30(3):156–163, May 1983.
5. J.W. Goodman. Statistical properties of laser speckle patterns. *IEEE Transactions on Ultrasonics, Ferroelectrics and Freq Control*, 33(6):754–758, 1986.
6. C.P. Loizou, C.S. Pattichis, C.I. Christodoulou, R.S.H. Istepanian, and M. Pantziaris. Comparative Evaluation of Despeckle Filtering In Ultrasound Imaging of the Carotid Artery. *IEEE Transactions on Ultrasonics, Ferroelectrics, and Frequency Control*, 52(10):1653–1669, Oct 2005.
7. Bibo Lu, Linlin Zhang, and Fuqiang Xing. Sar speckle reduction based on nonlocal means method. In *Proceedings of the 2010 Second International Conference on Computer Modeling and Simulation - Volume 02, ICCMS '10*, pages 156–159, Washington, DC, USA, 2010. IEEE Computer Society.
8. R. Martinsen, K. Kennedy, and A. Radl. Speckle in laser imagery: efficient methods of quantification and minimization. In *Lasers and Electro-Optics Society 1999 12th Annual Meeting. LEOS '99. IEEE*, volume 1, pages 354–355 vol.1, 1999.
9. O. Michailovich and A. Tannenbaum. Despeckling of Medical Ultrasound Images. *IEEE Transactions on Ultrasonics, Ferroelectrics and Frequency Control*, 53(1):64–78, Jan 2006.
10. J. Nascimento, J. Sanches, and J. S. Marques. An Unified Framework for Bayesian Denoising for Several Medical and Biological Imaging Modalities. In *Proceedings EMBC 2007*, pages 6268–6271, Lyon, France, Aug 2007. IEEE Engineering in Medicine and Biology Society.
11. G. Gilboa, N. Sochen, and Y. Zeevi. Variational denoising of partly textured images by spatially varying constraints. *IEEE Transactions on Image Processing*, 15(8):2281–2289, Aug 2006.
12. Peter C. Tay, Scott T. Acton, and John A. Hossack. Ultrasound despeckling using an adaptive window stochastic approach. In *Proc. of the Int. Conf. on Image Processing (ICIP 2006)*, pages 2549–2552, Atlanta, GA, USA, April 2006.
13. A. Buades, B. Coll, and J.M. Morel. A review of image denoising algorithms, with a new one. *Multiscale Modeling & Simulation*, 4(2):490–530, 2005.
14. C.I. Christodoulou, C.S. Pattichis, M. Pantziaris, and A. Nicolaides. Texture-based classification of atherosclerotic carotid plaques. *IEEE Transactions on Medical Imaging*, 22(7), 2003.
15. S.S. Mohamed and M. Salama. Prostate cancer spectral multifeature analysis using TRUS images. *IEEE Transactions on Medical Imaging*, 27(4):548–556, Apr 2008.
16. J. Thijssen et al. Computer-aided B-mode ultrasound diagnosis of hepatic steatosis: A feasibility study. *IEEE Transactions on Ultrasonics, Ferroelectrics and Frequency Control*, 55(6):1343–1354, Jun 2008.
17. A.T. Hope, P.H. Gregson, N.C. Linney, M.N. Schmidt, and M. Abdolell. Selecting and assessing quantitative early ultrasound texture measures for their association with cerebral palsy. *IEEE Transactions on Medical Imaging*, 27(2):228–236, Feb 2008.
18. T. Eltoft. Modeling the amplitude statistics of ultrasonic images. *IEEE Transactions on Medical Imaging*, 25(2):229–240, Feb 2006. Comparative Study.
19. R.W. Prager, A.H. Gee, G.M. Treece, and L.H. Berman. Decompression and speckle detection for ultrasound images using the homodyned k-distribution. *Pattern Recogn. Lett.*, 24(4-5):705–713, 2003.
20. P.M. Shankar. Ultrasonic tissue characterization using a generalized Nakagami model. *Ultrasonics, Ferroelectrics and Frequency Control, IEEE Transactions on*, 48(6):1716–1720, 2001.

21. V. Dutt and J. F. Greenleaf. Adaptive speckle reduction filter for log-compressed b-scan images. *IEEE Transactions on Medical Imaging*, 15(6):802–813, 1996.
22. S. Gupta, L. Kaur, R. C. Chauhan, and S. C. Saxena. A wavelet based statistical approach for speckle reduction in medical ultrasound images. *Medical and Biological Engineering and computing*, 42(2):189–192, 2004.
23. Y. Yu and S.T. Acton. Speckle Reducing Anisotropic Diffusion. *IEEE Transactions on Image Processing*, 11(11):1260–1270, Nov 2002.
24. Curtis R. Vogel. *Computational methods for inverse problems*. Frontiers in applied mathematics. 2002.
25. J.M. Sanches, J.C. Nascimento, and J.S. Marques. Medical image noise reduction using the sylvester-lyapunov equation. *IEEE Transactions on Image Processing*, 17(9):1522–1539, 2008.
26. J. Nascimento and J. Sanches. Total variation with automatic hyper-parameter estimation. In *Proceedings EMBC 2008*, pages 443–446, Vancouver, Canada, Aug 2008. IEEE Engineering in Medicine and Biology Society.
27. C. Sehgal. Quantitative relationship between tissue composition and scattering of ultrasound. *Acoustical Society of America Journal*, 94:1944–1952, October 1993.
28. J.W. Harris and H. Stocker. *Maximum Likelihood Method*, page 824. Handbook of Mathematics and Computational Science. Springer-Verlag, New York, 1998.
29. J. Hadamard. Sur les problèmes aux dérivées partielles et leur signification physique. *Princeton University Bulletin*, pages 40–52, 1902.
30. J.N. Besag. On the statistical analysis of dirty pictures. *J. R. Statist. Soc. B*, 48(3):259–302, 1986.
31. Stuart Geman and Donald Geman. Stochastic relaxation, gibbs distributions, and the bayesian restoration of images. pages 564–584, 1987.
32. T.K. Moon and W.C. Stirling. *Mathematical methods and algorithms for signal processing*. Prentice-Hall, 2000.
33. V. Arsigny, P. Fillard, X. Pennec, and N. Ayache. Log-Euclidean metrics for fast and simple calculus on diffusion tensors. *Magnetic Resonance in Medicine*, 56(2):411–421, Aug 2006.
34. S. Boyd and L. Vandenberghe. *Convex Optimization*. Cambridge University Press, Mar 2004.
35. Z. Shi and J. Shen. New Inexact Line Search Method for Unconstrained Optimization. *Journal of Optimization Theory and Applications*, 127(2):425–446, 2005.
36. J.C. Seabra, L.M. Pedro, J. Fernandes e Fernandes, and J.M. Sanches. A 3D Ultrasound-Based Framework to Characterize the Echo-Morphology of Carotid Plaques. *IEEE Transactions on Biomedical Engineering*, 56(5):1442–1453, May 2009.
37. L.M. Pedro, J.F. Fernandes, M.M. Pedro, I. Gonçalves, and N.V. Dias. Ultrasonographic risk score of carotid plaques. *European Journal of Vascular and Endovascular Surgery*, 24:492–498, December 2002.
38. C.H. Lee et al. Usefulness of standard deviation on the histogram of ultrasound as a quantitative value for hepatic parenchymal echo texture; preliminary study. *Ultrasound in Medicine & Biology*, 32(12):1817–26, 2006.
39. Y. Saijo, A. Tanaka, H. Sasaki, T. Iwamoto, E. Filho, M. Yoshizawa, and T. Yambe. Basic ultrasonic characteristics of atherosclerosis measured by intravascular ultrasound and acoustic microscopy. *International Congress Series*, 1274:116 – 121, 2004.
40. Timothy C. Strand Darwin T. Kuan, Alexander A. Sawchuk and Pierre Chavel. Adaptive noise smoothing filter for images with signal-dependent noise. *IEEE Transactions on Pattern Analysis and Machine Intelligence*, 7(2):165–177, March 1985.
41. R.W. Prager, A.H. Gee, G.M. Treece, and L. Berman. Speckle detection in ultrasound images using first order statistics. Technical Report CUED/F-INFENG/TR 415, Cambridge University, Cambridge, UK, 2002.
42. M. Nagao and T. Matsuyama. Edge preserving smoothing. *Computer Graphics and Image Processing*, 9(5):394–407, 1979.
43. T. Loupas, W. McDicken, and P. Allan. An adaptive weighted median filter for speckle suppression in medical ultrasonic images. *IEEE Transactions on Circuits and Systems*, 36:129–135, January 1989.

44. S. M. Ali and R. E. Burge. New automatic techniques for smoothing and segmenting sar images. *Signal Process.*, 14(4):335–346, 1988.
45. R. Dantas and E. Costa. Ultrasound speckle reduction using modified Gabor filters. *IEEE Transactions on Ultrasonics, Ferroelectrics and Frequency Control*, 54(3):530–538, Mar 2007.
46. T. Aysal and K. Barner. Rayleigh-Maximum-Likelihood Filtering for Speckle Reduction of Ultrasound Images. *IEEE Transactions on Medical Imaging*, 26(5):712–727, May 2007.
47. E.A. Krupinski K.S. Berbaum. The Medical Image Perception Society Update on Key Issues for Image Perception Research. *Radiology*, 253(1):230–233, 2009.
48. T. Hill. The first-digit phenomenon. *American Scientist*, 86:358–363, 1996.
49. J.M. Jolion. Images and benford’s law. *J. Math. Imaging Vis.*, 14(1):73–81, 2001.
50. J. Canny. A computational approach to edge detection. *IEEE Trans. Pattern Anal. Mach. Intell.*, 8(6):679–698, November 1986.
51. R. Ribeiro and J. Sanches. Fatty liver characterization and classification by ultrasound. In *IbPRIA '09: Proceedings of the 4th Iberian Conference on Pattern Recognition and Image Analysis*, pages 354–361, Berlin, Heidelberg, 2009. Springer-Verlag.
52. J. Seabra and A. Fred. Towards the development of a thyroid ultrasound biometric scheme based on tissue echo-morphological features. In *Biomedical Engineering Systems and Technologies, Communications in Computer and Information Science*, pages 286–298. Springer-Verlag Berlin Heidelberg, 2010.